Molecular Simulations of Thermal Transport Across Interfaces: Solid-vapor and Solid-Solid

Sohail Murad*[1] and Ishwar K.Puri[2]

[1]Department of Chemical Engineering

University of Illinois at Chicago

Chicago, IL 60607, USA

[2]Department of Engineering Science and Mechanics,

Virginia Tech

Blacksburg, Virginia 24061, USA

Submitted to

Molecular Simulation

December 2011

Abstract

Using molecular simulations, we have investigated heat transfer across the solid-fluid interface between water and silicon and silica wafers, and solid-solid interfaces in superlattices and thin solid films. The system set up has allowed us to focus on the resistance associated with both the fluid and solid interfaces. For instance, by maintaining the solid phase at a constant temperature we can focus solely on the fluid side resistance. Our results show that the thermal or Kapitza resistance at fluid side of the solid-fluid decreases significantly as the surface is made more hydrophilic. This is primarily due to increases in fluid adsorption and absorption at the surface, which enhance the intermolecular collision frequency at the interface. Increasing this frequency also reduces the dependence of thermal transport on variations in the interfacial temperature and pressure. Hence, decreasing the density diminishes the intermolecular collision frequency, which increases the thermal resistance. By maintaining the fluid at a constant temperature we have also examined the interface resistance on the solid side. Our results show that these interfacial resistances can diminish the wall heat flux by an order of magnitude in comparison with a hypothetical system for which the overall fluid–solid contact resistances are negligible. Finally, we consider the solid phase as a superlattice in which case the interfacial resistances produced between different solid layers can significantly lower the heat transfer. Our simulations show significant resistance to thermal transport between thin films of the solid phase that constitute the superlattice, providing insight into how a superinsulator can be designed.

Keywords: thermal transport; interfaces; solid-solid; fluid-solid

*Address correspondence to this author. E-mail: murad@uic.edu.

Phone: (312)996-5593.

1. Introduction

The contact resistance problem between dissimilar or bonded substrates is particularly important at the nanoscale, since the length scales associated with the structures and energy carriers become comparable[1]. The thermal management of electronic packaging of thermo-electrics[2], nanofabrication[3], and heat transfer though microchannels[4] has prompted atomic-level investigations of this resistance. When thermal energy is transported through a solid-fluid interface of area A, it produces a temperature discontinuity across the boundary[5]. If the heat flow Q' across the interface is small, the temperature difference across the interface ΔT is thought to be proportional to it. The effective thermal resistance $\Delta T/Q'$ is typically expressed as the Kapitza resistance[6, 7],

$$R = A\,\Delta T/Q' \text{ (m}^2\text{ K/W)}. \tag{1}$$

The first measurements of R were made by Kapitza for metal surfaces suspended in He II (the superfluid phase of ^{4}He) in the temperature range between 1.6-2.12 K. These and other similar experiments involving other substances and temperatures suggest that $R \propto T^{\alpha}$, where α is an empirical exponent. The Kapitza resistance can then be represented as the reciprocal of the interfacial conductance[8], i.e., $R = 1/G = AdT/Q'$.

Like other transport and thermodynamic properties, the thermal behavior of nanostructured interfaces, e.g., in nanoelectronic devices or across nanometer scale point like constrictions, cannot be simply inferred by extrapolating bulk behavior to the smaller scales. Phonons, that are quanta of lattice vibrational energy, play a major role in determining the thermal and electrical resistances of a material and the effects of the interfacial resistance can be explained in the light of phonon scattering[8, 9]. Nanoscale thermal transport differs from transport in bulk materials because the mean free path for

phonon scattering can be large compared to device dimensions[10]. The thermal resistance arises due to the large impedance to the passage of thermal phonons across a solid-fluid interface. The impedance, which is the product ρc of the density and sound velocity or depends upon ρ alone depending upon the model used, can be many orders of magnitude greater for a solid than a fluid [6,11]. Due to the acoustic mismatch, a large fraction of the phonons impinging upon such an interface from both sides are unable to pass through it.

The above understanding of phonon behavior suggests several strategies to reduce the mismatch at the interface, thus decreasing R and increasing Q/A, as follows. (1) Since ρc and ρ both increase with pressure, increasing the fluid pressure should facilitate better acoustic matching, thus lowering R. (2) A more solid-like interface could be created by adsorbing and ordering additional fluid molecule layers [6,12], e.g., by making the surface more hydrophilic[13, 14]. Further, as a fluid is constrained into smaller pore spaces, the collision frequency of its molecules increases above the corresponding rate in the bulk phase, which enhances thermal transport[15]. Therefore, we can hypothesize that the addition of an *absorption* fluid layer within the nanopores of a hydrophilic solid-fluid interface to the adsorption layer adjacent to it should further reduce R_k. This should also induce a weaker dependence of thermal transport on temperature and pressure.

As discussed above, several previous studies (including ours) have examined the influence of the fluid–solid impedance and the impact of hydrophilic fluid layering on the fluid–side thermal resistance. The overall interfacial resistance can be considered to be a combination of the fluid and solid thermal resistances R_f and R_s for a solid wall of thickness L that separates two fluid reservoirs, one at a uniform hot temperature $T_{f,h}$ and the other at a corresponding cold temperature $T_{f,c}$. These are schematically described in

Fig. 1 where the temperature variables used are also defined. The mean wall temperature $T_m = (T_{f,h}+T_{f,c})/2$. If $R = 0$, the temperature gradient across the wall $T'_1 = (T_{f,h}-T_{f,c})/L$. Finite thermal resistances $R_{f,h}$ and $R_{f,c}$ on the hot– and cold–side fluid interfaces produce the temperature discontinuities ΔT_h and ΔT_c, and decrease this gradient to $T'_2 = (T_{h,i}-T_{c,i})/L$, where $T_h<T_{f,h}$ and $T_c>T_{f,c}$. Effects on the solid side due to the formation of subnanometer thermal boundary layers, that are our focus herein, have not been usually considered significant, and have been attributed to the finite solid-side thermal conductivity[16]. When the solid–side resistances $R_{s,h}$ and $R_{s,c}$ across these δ_t thick thermal boundary layers are also accounted for, the bulk wall temperature on the hot side is lowered by $\Delta T_{s,h}$ and similarly raised on the cold side by $\Delta T_{s,c}$, as shown in Fig. 1. Hence, the temperature gradient within the solid wall declines further to $T'_3 = (T_{s,h}-T_{s,c})/(L-2\delta_t)$. Employing the empirical Fourier heat conduction relation

$$q' = kT', \tag{2}$$

where $k = k_m$ is evaluated at T_m, it is clear that $q'_3 < q'_2 < q'_1$ for these three cases. These effects can be expected to become significant in systems in which the thermal boundary layer is a non-negligible fraction of the total wall thickness.

2. Models and Method

Our studies that targeted the interfacial resistance on the fluid side with silicon walls consisted of 1024 particles in a basic cyclically replicated parallelepiped that contains two walls. Each wall consists of 256 Si atoms (or 4×4 unit cells) that are placed at their normal equilibrium sites in a Silicon crystal. For walls consisting of β-cristobalite silica (SiO_2) we had 2560 particles in a basic cyclically replicated parallelepiped reservoir that

contains two walls within it[17,18]. Each wall in this case consists of 762 atoms (254 Si and 508 O atoms) placed at their normal equilibrium sites in a β-cristaobalite silica (SiO_2) crystal[19], as shown in Fig. 2. The molecules constituting the walls are tethered to these equilibrium sites and allowed to vibrate using a simple harmonic potential. Initially, water molecules are uniformly distributed in the two reservoirs that are placed on either side of these walls. The axial (x-wise) dimension of the system is much larger than the transverse y and z directions to facilitate the simultaneous simulation of both bulk and molecular-scale characteristics. Thus, while the walls influence small portions of the fluid adjacent to them, the remaining fluid in the reservoirs exhibits bulk properties. The volumes of the reservoirs between the walls are held equal and fixed to maintain a water density ρ of 975 kg/m^3 for most simulations, although we also conduct additional simulations for half this density. All molecules are provided with initial Gaussian velocity distributions in the solid and fluid regions. We impart different hot and cold temperatures T_h and T_c to the silica walls (on average using a Gaussian thermostat), which results in an average fluid temperature $T_{av,f}=(T_h+T_c)/2$ that varies due to the corresponding heat flux[11]. The (N,V,T) simulations proceed with a uniform step size of 1 fs and are allowed to equilibrate to achieve an energy minimum state. We report results for simulations that have progressed by 2×10^6 time steps to 2 ns, i.e., after the system has reached a steady state.

The molecular dynamics algorithm uses the quaternion method with a fifth-order Gear predictor–corrector algorithm for translational motion and a fourth-order predictor–corrector algorithm for rotational motion[20,21]. Intermolecular interactions are described by the potential model $u_{ij} = 4\varepsilon_{ij}((\sigma_{ij}/r_{ij})^{12} - (\sigma_{ij}/r_{ij})^{6}) + (q_i q_j)/r_{ij}$, where σ_{ij} and ε_{ij} denote

the LJ interaction parameters, r_{ij} the scalar distance between sites i and j, and q_i and q_j the charges on these sites (since water contains a partial positive charge for H and negative for O, and SiO_2 also has partial charges for both Si and O, making it strongly hydrophilic)[22]. The parameters σ and ε closely represent experimental geometries, energies of ion–water complexes, and energies of solvation[23]. A more accurate potential model for Si (the Stillinger-Weber model) was not used here[24]. The S-W model uses three body interactions to enforce the correct coordinated tetrahedral bonded structure of Si. We were able to enforce it by tethering the Si atoms to their equilibrium site; therefore the simpler LJ model (which is computationally less expensive) was an acceptable alternative here. Lorentz-Berthelot mixing rules are used to model cross interactions[21] and the reaction field method for long-range interactions[25, 26] with parameters corresponding to the average state conditions of the systems and a potential cut off of 9.5Å. Although the reaction field method is intended for homogeneous systems, recent studies have found that it works well for nonhomogeneous systems as well[27]. For example, the more accurate particle-particle mesh method has been found to provide results comparable with the reaction field method. We note in the context of the larger cutoff distance used herein that our previous studies that also involve nonhomogeneous systems [17] have shown that long range interactions do not seem to significantly contribute to transport processes in the types of systems being investigated here. Water is modeled after the SPC potential[28] and the SiO_2 wall molecules using a model that correctly represents surface wettability[29]. Other potential models for SiO_2 are also available[19,30]. Since our goal is to demonstrate system behavior rather than make quantitative comparisons, we have chosen a simpler but realistic model for computational efficiency.

For studies that focused on the solid interfacial layer, the method was essentially the same, but the fluid phase temperatures were held constant, as shown in Figure 3. In addition we also studied walls which were composites of Si and an arbitrarily defined material M, with molecular diameters different than that of silicon (see results for further details).

3. Results and Discussions

We first discuss the studies that focus on the fluid interfacial layer. Here, the walls are maintained at constant high and low temperatures, as shown in Fig. 2. The spatial distributions of the water and silica densities and of the temperature for a representative system are presented in Fig. 4 (a) for the case with silica walls. We segment the simulation domain into 138 transverse strips along L_x and average the local temperature and density of SiO_2 and H_2O molecules in each segment. Since the SiO_2 surfaces are both hydrophilic and naturally nanoporous due to the configuration of each silica cell, the water molecules adjacent to each wall organize into an absorption layer that penetrates the silica face, and is preceded by two adsorption layers on the fluid side. The absorption layer, which infuses ≈0.5 nm into the silica wall, has a thickness of roughly two molecular diameters. The successive adsorbed water layers are each roughly four molecular diameters thick. The adsorption layers on either side of a reservoir hold a bulk layer in between them that has a nearly constant water density, i.e., the local and bulk densities are similar in this region. The overall heat flux in the system is determined from the temperature distribution in the bulk layer, i.e.,

$$Q'/A = k_{T'}(dT/dx)_{T'}, \qquad (3)$$

where both the gradient and thermal conductivity k_T [31] are calculated at the average bulk temperature T'. Q´ was obtained from eqn. (3) by measuring the temperature gradient in the fluid section and obtaining the thermal conductivity of water from data the NIST web-book[32]. This value was also validated by comparing with the energy supplied to the hot wall and removed from the cold wall to maintain the wall temperatures at the desired values. We evaluate R_k using Eqs. (1) and (3) and by calculating ΔT_i across the fluid-side edge of the hybrid absorped-water/SiO_2 nanoporous layer at x_s and the wall-side face of the adsorption layer at x_f that precedes it, as indicated in Fig. 4. The hybrid solid/fluid mass has a temperature closer to that of the purely solid interface than for surfaces that do not absorb water[11], which helps lower ΔT_i and R_k. The temperature profiles for such a surface (silicon walls) are shown for comparison in Figure 4 (b). For the ρ = 975 kg m^{-3} simulations, ΔT_i ~20-40K for a liquid/vapor mixture (<348K), for liquid ~100-110K, and ~50-110K in the supercritical fluid region (>648K). The variation of the Kapitza resistance with respect to the interface temperature at x_f is presented in Fig. 5 for regions containing coexisting liquid and vapor phases, liquid, or supercritical fluid. The values of R_k transform smoothly across the transitions between the three regions. Since the simulations are isochoric, an increase in the temperature also corresponds to an increase in pressure [33,34]. Figure 4 also shows that the thermal conductivity of the interfacial layer is much lower than that of the bulk fluid in this system.

Overall, we find that the results are consistent with the empirical expression [6,7] $R_k \propto T_i^{-1.17}$, confirming that $R \propto T^{-\alpha}$. As expected, the more hydrophilic SiO_2 surfaces that include an absorption water layer have a smaller value of α than Si interfaces[11]. The thermal resistance for the adsorbing/absorbing interfaces are smaller and have a weaker

dependence on temperature than for less hydrophilic Si interfaces[11]. The interfacial - resistance across a liquid/vapor mixture can be three times larger than for a supercritical fluid. This is intuitive, since the molecular collision frequency at a supercritical fluid interface is higher than for one consisting of liquid or a liquid/vapor mixture. For a similar interface temperature, R_k should increase with decreasing density since the collision frequency would diminish. This is corroborated by the results presented in Fig. 5.

We now discuss results for simulations which focus on the solid interfacial layer. As mentioned earlier these studies were performed by maintaining the two fluid sections at constant high and low temperatures (see Figure 3a). The distributions of the simulated fluid and solid temperatures T_f and T_s, and the number of water molecules N thus averaged are presented in Fig. 6 for a typical system. The intermolecular attractive (van der Waals) forces between Si atoms and water molecules lead to the layering of fluid on the solid surfaces, as observed through the spatial variation of N adjacent to the four fluid–solid interfaces[11,35,36] . The water density is constant in the bulk of the hot and cold reservoirs. The Kapitza resistance between the H_2O molecules and the Si atoms produces the temperature discontinuities ΔT_c and ΔT_h on the cold– and hot–sides of each wall, where $\Delta T_c > \Delta T_h$. Once a temperature difference is imposed for a specific case, so is the heat flux. The cold–side fluid thermal resistance $R_{f,c}$ is typically larger than the resistance on the hot side $R_{f,h}$ [6,9,35], since $R \propto \Delta T$ (from Eq. (1)).

Figure 6 also shows that thermal boundary layers are formed within each Si wall adjacent to its cold and hot surfaces. For all of the cases considered, the thickness of this boundary layer $\delta_t \approx 0.45$ nm, i.e., it is not much larger than a Si atom layer. The walls are

3.25 nm thick so that the boundary layers constitute almost 28 percent of the total wall dimension, which would be the norm in most nanosystems. The temperature drops across these thermal boundary layers $\Delta T_{s,c}$ and $\Delta T_{s,h}$ decrease the bulk wall temperature gradient T'_3 in the wall as shown schematically in Figs. 1 and 6. Since $T'_1 > T'_3$ (see discussion preceding Eq. 2 and Fig. 1 for definitions of these variables), it is also apparent from Eq. (2) that $q'_3 < q'_1$. (Here, the thermal conductivity k_m is calculated[37] at the simulated mean wall temperature T^*_m.) As illustrated in Fig. 6, it differs from the value of the overall mean temperature T_m based on averaging T_h and T_c. Averaging the two values for $\Delta T_{s,c}$ and for $\Delta T_{s,h}$ allows us to determine the mean solid-side thermal resistances $R_{s,c}$ and $R_{s,h}$ that are formed due to these thermal boundary layers. The effect of $R_{s,c}$ and $R_{s,h}$ is to lower the effective thermal conductivity in the boundary layer. If the temperature gradient in the bulk of the solid wall is compared with that in the boundary layer, the ratio of the thermal conductivity in the boundary layer to that in the bulk $k_\delta/k_m \approx 0.52$ on average for the nine cases we simulated. Table 1 shows results for these variables as the system parameters are varied.

The averaged overall temperature drop $\Delta T_s = (\Delta T_{s,c} + \Delta T_{s,h})/2$ for the cases we investigated correlates with the bulk heat flux according to the relation $\Delta T_s \approx 10^{-6}\, q'^{0.63}_3$. Due to the existence of the subnanometer resistances associated with the thermal boundary layers, the bulk heat flux is significantly smaller than the heat that could have been transferred if no such resistances had existed (for instance, in a macroscale system) by an order of magnitude so that $q'_3/q'_1 \approx O(10^{-1})$. In contrast to the behavior of the fluid side resistances $R_{f,c}$ and $R_{f,h}$ that vary inversely with the interface temperature[5,6,11,35]], neither $R_{s,c}$ nor $R_{s,h}$ correlate well with either the reservoir or mean wall temperatures.

Finally we also carried out simulations in which the solid walls were composite with two or multiple layers (with alternating layers of Si and an arbitrary molecule similar to Si but with a larger molecular diameter[38,39] M_i—see Figure 3b). Figure 7 presents the temperature profiles thus obtained in a typical simulation with a two and six layer composite wall. The temperature distribution reveals the presence of thermal boundary layers adjacent to the solid-fluid and solid-solid interfaces. These boundary layers form resistances which lower the effective thermal conductivity. The boundary layer thickness $\delta_t \approx 2\Delta x$ or 0.3 nm, which is roughly the width of a single atomic layer. Since it is identical in both the Si and M_i layers, the heat flux Q through the wall is constant. Using the empirical Fourier conduction law, $Q = -k\nabla T$, where k denotes the thermal conductivity, the lower effective k for the Si wall is apparent through its steeper temperature gradient ∇T as compared to that through M_i. Placing several thermal resistances in series in a composite Si-M_i six-layer wall further distorts the temperature profile, since phonon scattering now occurs at multiple Si-M_i interfaces. This decreases the value of Q and thus the overall value of k as presented in Table 2. A series resistance model, such as one presented in Fig. 1, can be used to determine an effective thermal conductivity for the entire system. This can be particularly useful for multilayer systems. It can also be used to elucidate the length dependence of the interfacial thermal resistance when the system dimension is smaller than the phonon mean free path.[40]

As seen through the LJ (6–12) potential model, increasing σ augments the intermolecular interactions between two neighboring M_i atoms or sites. The resulting decrease in the effective interparticle distance augments thermal transport. The heat flux through homogeneous walls comprised of a single material monolayer increases with

increasing σ according to the empirical relation $Q \propto \sigma^{3.64}$, i.e., the thermal transport through the modified materials scales roughly with their atomic volumes. Figure 8 compares the relative heat flux Q/Q^* for systems investigated (normalized with the flux for a wall with one composite bilayer) as a function of the wall composition and the overall temperature difference across it. A nearly 17% increase in the molecular size for M_i leads to a nearly 80% increase in Q for a 645 K temperature difference across the wall. Increasing the number of composite Si-M_i layers in the solid walls leads to a higher impedance of the heat transfer. A six-bilayer Si-M_i wall conducts less heat than a corresponding single bilayer composite wall of the same thickness. It has been noted[41] that the significant changes in the thermal conductivity[42,43] that we have also observed cannot be accounted for by the interface resistance alone. Our simulations offer an explanation, i.e., the decrease in thermal conductivity can be attributed in part to the thermal boundary layers within the solid layers, which encompass a relatively wide thickness around the contact interface between two solid crystals. This impedance is also sensitive to the temperature difference across the wall and thus the interfacial temperature. Lowering the temperature difference makes a multilayer wall less effective in transferring heat. The heat transferred across a six-layer wall is 5% smaller than the flux across a bilayer wall when the temperature difference across it is 806 K. For a 645 K difference the flux is reduced by 15% but this decrease in flux is 41% at 484 K.

Conclusions

The Kapitza resistance to thermal transport across a solid-fluid interface can be decreased by making the interfacial fluid layers more solid-like. This can be accomplished by increasing the fluid pressure or by adsorbing and ordering additional

fluid molecule layers by making the surface more hydrophilic. While R_k decreases with increasing temperature, which for our isochoric simulations corresponds to increasing pressure, on an overall basis, it increases during the transition through phases (liquid-vapor to liquid and liquid to supercritical fluid). It is also inversely proportional to the heat flux.

The much smaller temperature gap for silica interfaces in comparison with silicon membranes, which are not as hydrophilic and thus do not cause water to be strongly adsorbed on the membrane surface, provide evidence of this enhanced thermal transport. The combination of the successive absorption/adsorption layers creates conditions that promote ballistic phonon conduction by ordering the interfacial fluid molecules as adjacently placed beads[44] so that the local properties assume a weaker dependence on pressure and temperature[45]. Decreasing the density diminishes the intermolecular collision frequency thus increasing R_k.

We have also shown that enhanced impedance to nanoscale thermal transport by subnanometer thermal boundary layers formed at the interfaces of superlattices is caused by two simultaneous effects, namely (1) the interfacial resistance between two solid phases of a superlattice, and (2) the thermal boundary layers that are formed within each phase adjacent to these interfaces. This observation can have significant design implications for semiconductor and related electronic devices that dissipate energy as heat. For example, depending upon the desired outcome, it would be advantageous to have composite films constructed in several alternating layers to inhibit heat transfer, but have fewer layers present if the thermal transport is to be enhanced. This facet has been not clearly discussed in the previous literature.

Acknowledgements:

SM was supported by a grant from the National Science Foundation (CBET 0730026).

Table 1: List of simulation cases corresponding to various overall temperature differences with the corresponding imposed hot– and cold–side reservoir temperatures T_h and T_c, and the overall and simulated mean wall temperatures T_m and ΔT^*_m. For each case, the simulated heat flux q'_3 across the solid walls is based on the temperature gradient T'_3 and the thermal conductivity k_m *of the bulk fluid*.

Case	T_h	T_c	T_m	T^*_m	$\Delta T_{s,h}$	$\Delta T_{s,c}$	q_3 $\times 10^{11}$	q_3/q_1	$R_{s,h}$ $\times 10^{11}$	$R_{s,c}$ $\times 10^{11}$	se $\times 10^{12}$	k_δ / k_m
I	1210	403	806	983	63.4	63.8	9.33	0.115	6.85	6.80	4.56	0.43
II	968	565	766	895	43.5	50.2	4.53	0.109	11.1	9.61	3.72	0.64
III	887	565	726	753	36.5	46.4	2.87	0.137	13.1	9.29	1.18	0.45
IV	806	484	645	681	26.7	37.5	4.32	0.053	8.11	7.13	2.67	0.60
V	726	403	565	609	30.8	35.1	6.46	0.070	7.18	5.65	2.48	0.62
VI	806	565	685	701	23.6	31.9	5.10	0.130	6.24	4.63	4.66	0.58
VII	726	484	605	629	21.8	32.7	2.64	0.059	12/4	8.26	2.46	0.38
VIII	645	484	565	565	16.2	22.6	3.11	0.065	6.02	4.92	1.67	0.51
IX	565	403	484	488	15.3	18.7	2.21	0.078	10.2	7.31	2.67	0.50

Figure Captions;

Figure 1: Schematic diagram of the thermal resistance across fluid–solid interfaces. A solid wall of thickness L and mean temperature T_m separates two fluid reservoirs at uniform cold and hot temperatures $T_{f,c}$ and $T_{f,h}$. The thermal resistances $R_{f,h}$ and $R_{f,c}$ on the hot– and cold–side fluid interfaces produce the temperature discontinuities ΔT_h and ΔT_c. The corresponding solid–side resistances $R_{s,h}$ and $R_{s,c}$ across δ_t thick thermal boundary layers produce the temperature differences $\Delta T_{s,c}$ and $\Delta T_{s,h}$. If there were no thermal resistances, the temperature gradient across the solid would be T'_1 and greater than T'_3, which is the gradient induced by the combined resistances (including the wall resistance $(L-\delta_t)/k_m$ for the latter case).

Figure 2: (a) top. Schematic illustration of the simulation system with the dimensions $L_x \times L_y \times L_z = 12.14 \times 2.036 \times 2.036$ nm with Silicaon walls. (b). bottom. Schematic illustration of a simulation system with the dimensions $L_x \times L_y \times L_z = 11.3 \times 2.842 \times 2.842$ nm. The hot and cold side SiO_2 interfaces (on the right and left, respectively) enclose water in between them. The cutout in the figure illustrates the SiO_2 structure.

Figure 3: Schematic diagram of the MD simulations for solid interface resistance studies. (a) Top. Shows the setup for a homogenous thin film consisting of silicon crystals with dimensions, $L_x = 20.99$ nm, and $L_y = L_z = 2.172$ nm. (b) Bottom. Shows walls with bilayer and six-layer composite Si (or M_1)-M_i superlattice walls. The domain dimensions are $L_x = 20.99$ nm, and $L_y = L_z = 2.172$ nm.

Figure 4: (a) Top. The dimensionless molecular distributions ρ^* of H_2O, and summed Si and O_2 atoms (represented respectively by the symbols ○ and □), and temperature distribution T^* (◇). The domain is segmented into 138 strips along L_x represented by x^*. Multiplying ρ^* by 3.961 mol/l and T^* by 806 K provides the corresponding dimensional quantities. The water adsorption (identified by dashed ovals) and absorption layers (identified as continuous ovals) adjacent to the four interfaces are identified, as is the bulk water layer indicated by closed symbols (●) in between the two walls that has an almost constant molecular distribution. (b) Bottom. The dimensionless temperature distribution T^* for Cases I(a) and I(b), represented respectively by the symbols □ and ○. Multiplying T^* by 800K results and x^* by 0.088 nm provides the corresponding dimensional quantities.

Figure 5: Variation of the Kapitza resistance with respect to the interface temperature. The liquid and vapor, liquid and supercritical regions are indicated for the cases

investigated. The closed symbols (●) refer to a density ρ = 975 kg m^{-3}, and the open symbols are for half that density.

Figure 6: The temperature profiles in the solid and fluid T_s and T_f, and the numbers of water molecules in the hot and cold fluid reservoirs. The segment numbers on the abscissa multiplied by 0.152 nm return the axial distance. The dimensionless temperature ordinate multiplied by 806.46 K provides the local temperature.

Figure 7: The temperature profiles for single bilayer (a) and six-bilayers composite walls. The segment numbers on the abscissa multiplied by 0.152 nm return the axial distance. The dimensionless temperature ordinate multiplied by 806.46 K provides the local temperature.

Figure 8: Relative heat flux Q/Q^* as a function of the superlattice wall composition, i.e., material and number of layers, and the temperature difference across it.

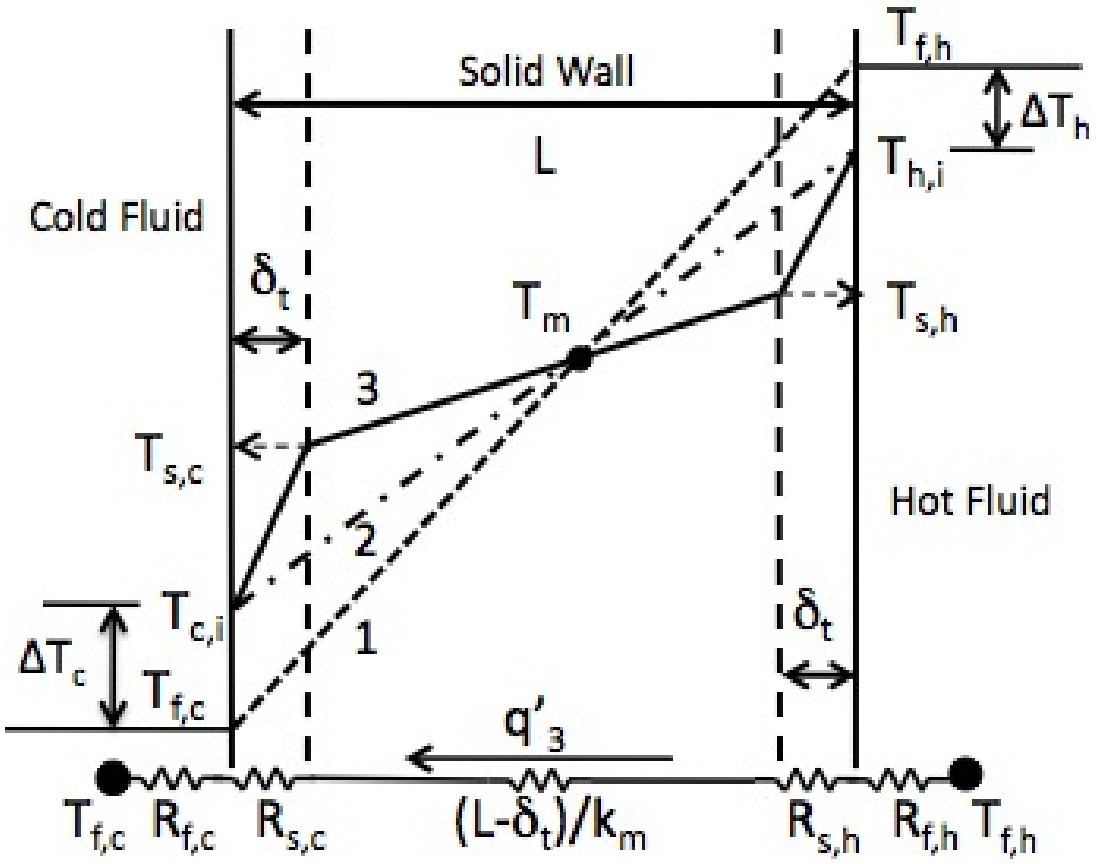
Solid Wall
L
Cold Fluid
Hot Fluid
$T_{f,h}$
ΔT_h
$T_{h,i}$
δ_t
T_m
$T_{s,h}$
3
$T_{s,c}$
2
1
$T_{c,i}$
ΔT_c
$T_{f,c}$
δ_t
q'_3
$T_{f,c}$ $R_{f,c}$ $R_{s,c}$ $(L-\delta_t)/k_m$ $R_{s,h}$ $R_{f,h}$ $T_{f,h}$

Figure 1

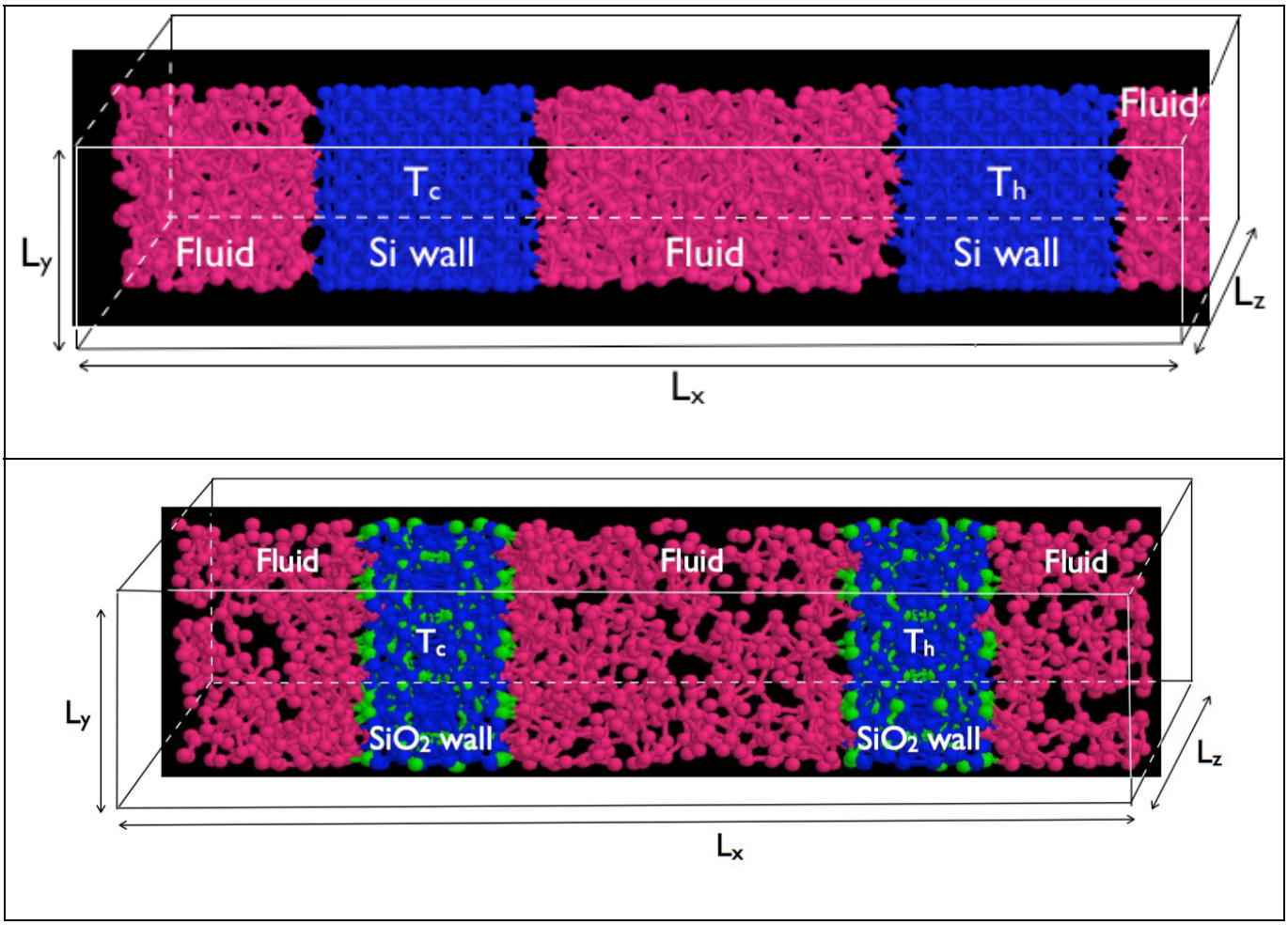
Fluid
T_c
T_h
Fluid
Si wall
Fluid
Si wall
L_y
L_z
L_x
Fluid
Fluid
Fluid
T_c
T_h
SiO_2 wall
SiO_2 wall
L_y
L_z
L_x

Figure 2

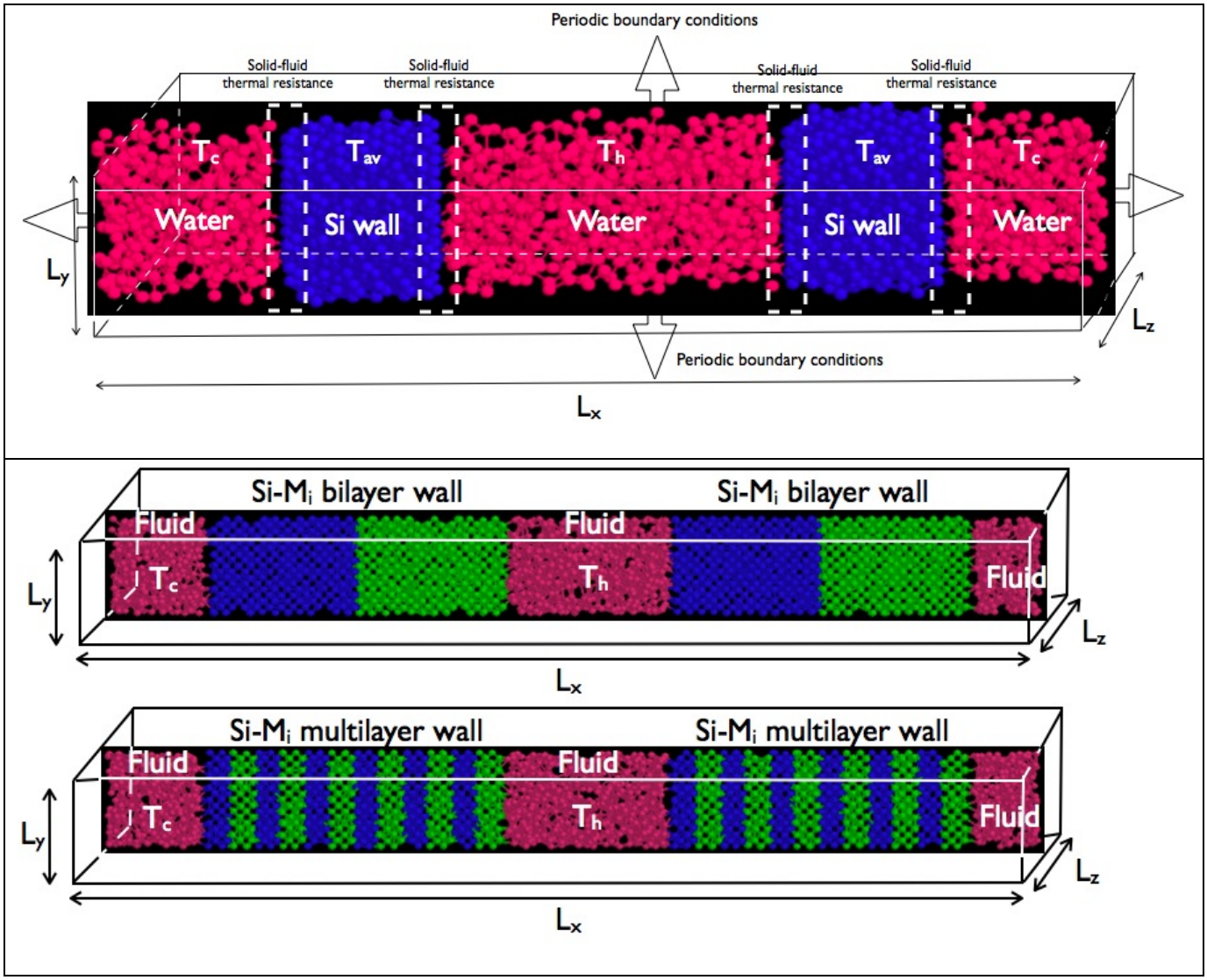
Periodic boundary conditions
Solid-fluid thermal resistance
Solid-fluid thermal resistance
Solid-fluid thermal resistance
Solid-fluid thermal resistance
T_c
T_{av}
T_h
T_{av}
T_c
Water
Si wall
Water
Si wall
Water
L_y
L_z
Periodic boundary conditions
L_x
Si-M_i bilayer wall
Si-M_i bilayer wall
Fluid
Fluid
Fluid
T_c
T_h
L_y
L_z
L_x
Si-M_i multilayer wall
Si-M_i multilayer wall
Fluid
Fluid
Fluid
T_c
T_h
L_y
L_z
L_x

Figure 3

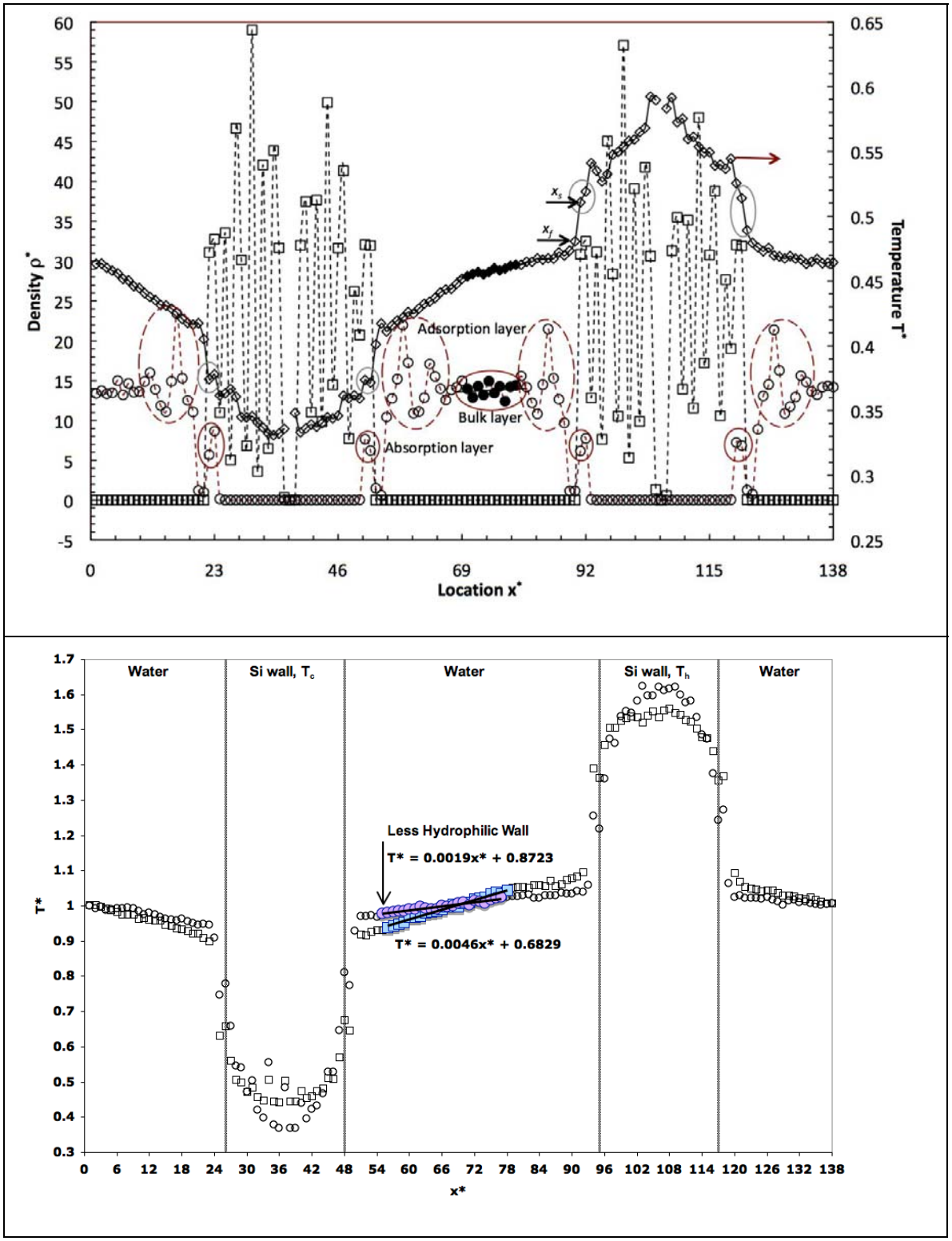
Density ρ*
Temperature T*
Location x*
Adsorption layer
Bulk layer
Absorption layer
x_s
x_f
Water
Si wall, T_c
Water
Si wall, T_h
Water
Less Hydrophilic Wall
T* = 0.0019x* + 0.8723
T* = 0.0046x* + 0.6829
T*
x*

Figure 4

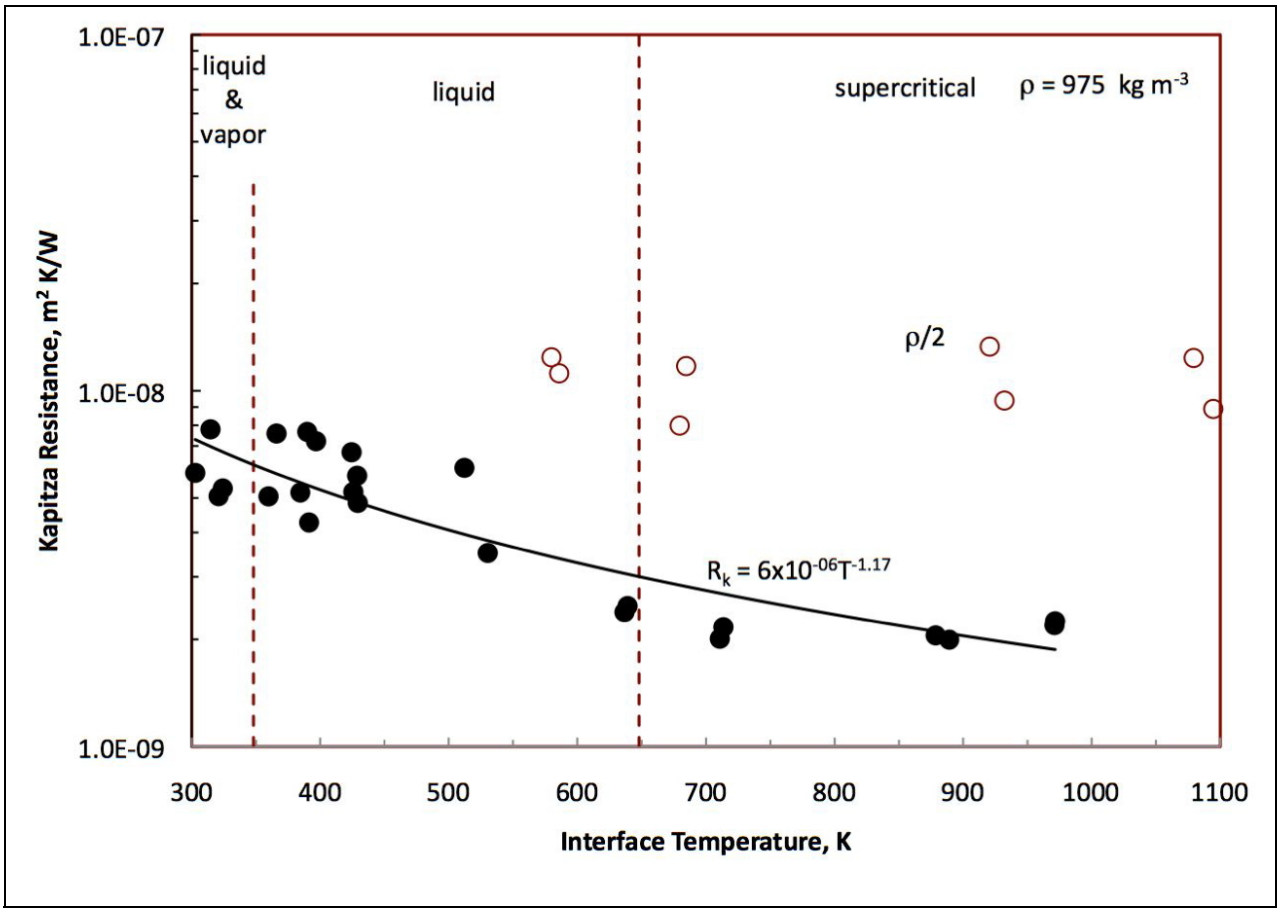
1.0E-07
1.0E-08
1.0E-09
liquid
&
vapor
liquid
supercritical
ρ = 975 kg m-3
ρ/2
Rk = 6x10-06T-1.17
Kapitza Resistance, m2 K/W
300
400
500
600
700
800
900
1000
1100
Interface Temperature, K

Figure 5

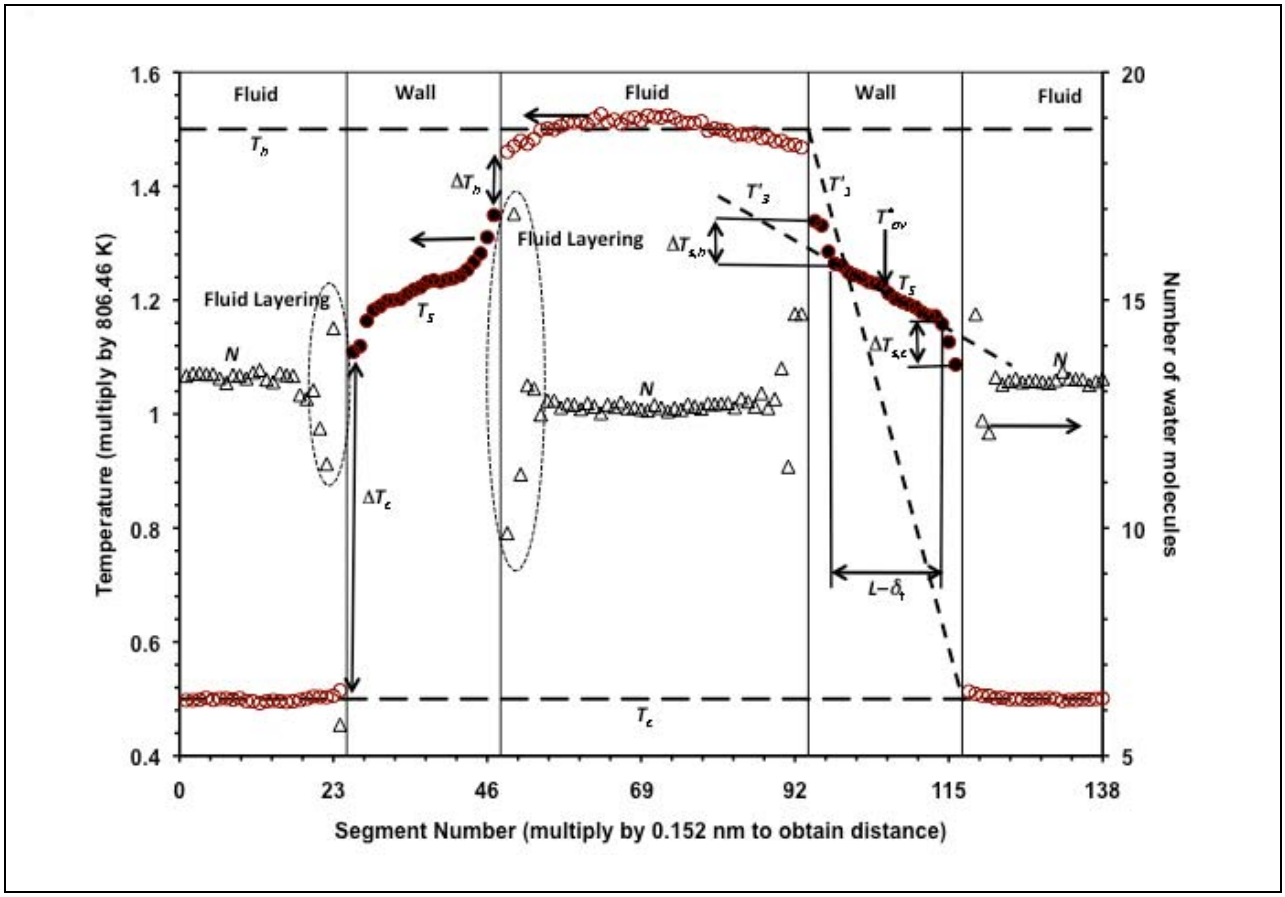
Fluid
Wall
Fluid
Wall
Fluid
Fluid Layering
Fluid Layering
N
N
N
Temperature (multiply by 806.46 K)
Number of water molecules
Segment Number (multiply by 0.152 nm to obtain distance)
1.6
1.4
1.2
1
0.8
0.6
0.4
20
15
10
5
0
23
46
69
92
115
138

Figure 6

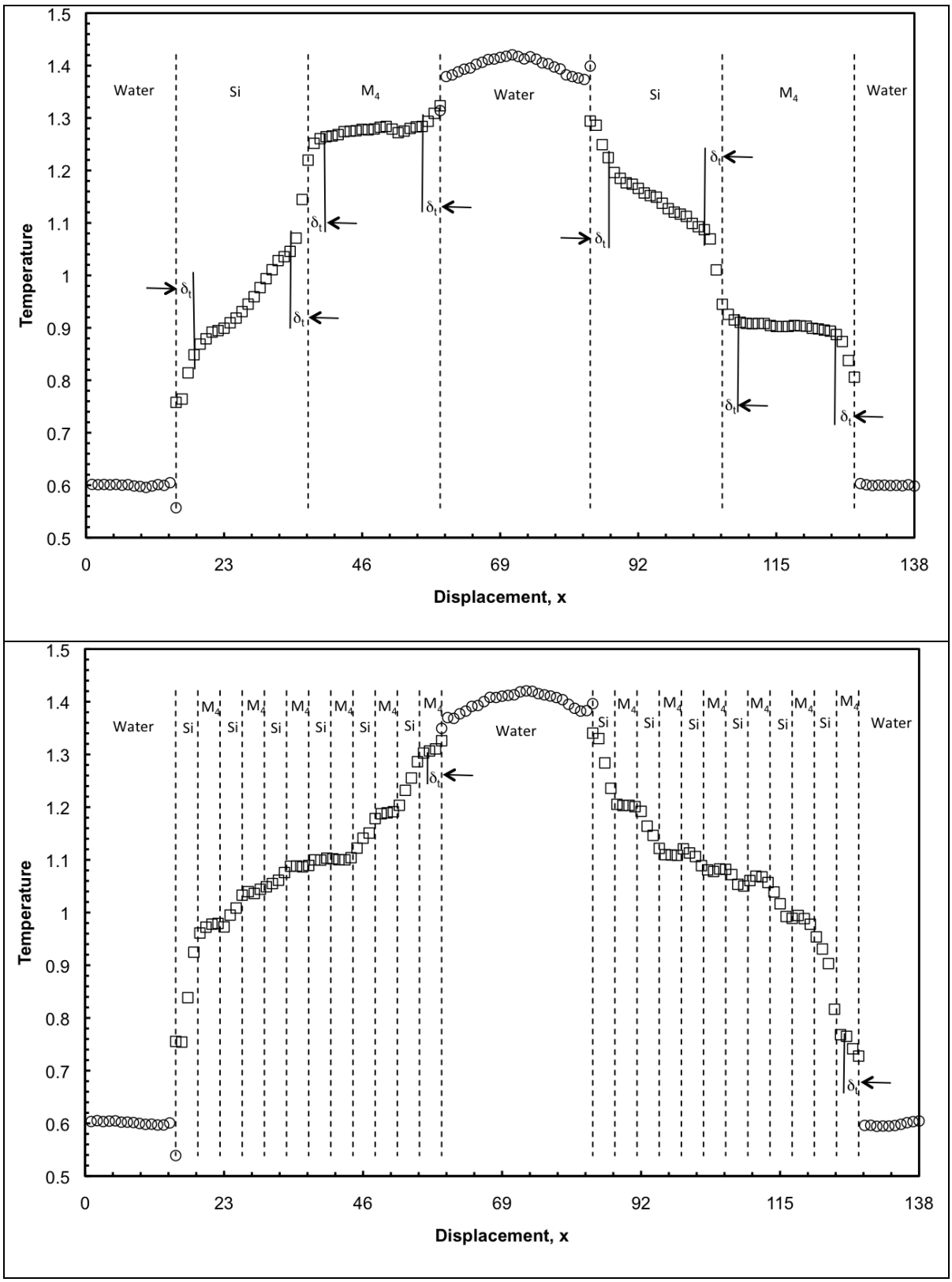
Water
Si
M4
Water
Si
M4
Water
Temperature
Displacement, x
0
23
46
69
92
115
138
0.5
0.6
0.7
0.8
0.9
1
1.1
1.2
1.3
1.4
1.5
δt

Figure 7

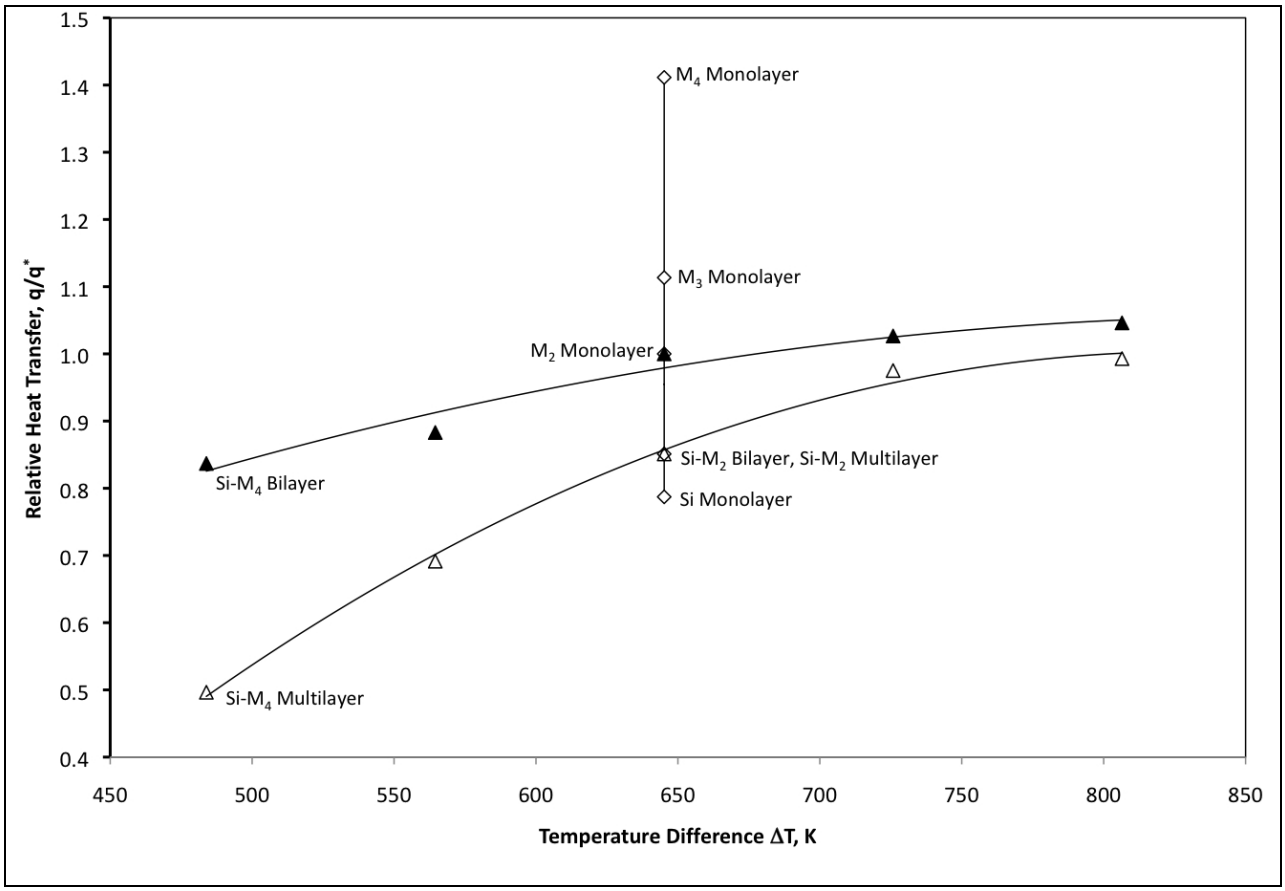
1.5
1.4
1.3
1.2
1.1
1.0
0.9
0.8
0.7
0.6
0.5
0.4
Relative Heat Transfer, q/q*
450
500
550
600
650
700
750
800
850
Temperature Difference ΔT, K
M4 Monolayer
M3 Monolayer
M2 Monolayer
Si-M4 Bilayer
Si-M2 Bilayer, Si-M2 Multilayer
Si Monolayer
Si-M4 Multilayer

Figure 8

References

1 ET Swartz, RO Pohl: Thermal-boundary resistance. Reviews of Modern Physics 61 (1989) 605-68.

2 J Darabi: Micro- and nanoscale heat transfer: Challenges and opportunities. Heat Transfer Engineering 23 (2002) 1-2.

3 G Chen: Particularities of heat conduction in nanostructures. Journal of Nanoparticle Research 2 (2000) 199-204.

4 JR Thome: The new frontier in heat transfer: Microscale and nanoscale technologies. Heat Transfer Engineering 27 (2006) 1-3.

5 PL Kapitza: The Study of Heat Transfer in Helium II. Journal of Physics, USSR 4 (1941) 181.
6GL Pollack: Kapitza Resistance. Reviews of Modern Physics 41 (1969) 48-81.

7 RA Ferrell, JK Bhattacharjee, SI Mukhin: Theory for normal state critical Kapitza resistance of He-4. Low Temperature Physics 24 (1998) 76-77.

8 LJ Challis: Kapitza resistance and acoustic transmission across boundaries at high frequencies. Journal of Physics C: Solid State Physics 7 (1974) 481-95.

9 J-L Barrat, F Chiaruttini: Kapitza resistance at the liquid-solid interface. Molecular Physics 101 (2003) 1605-10.

10 K Schwab, EA Henriksen, JM Worlock, ML Roukes: Measurement of the quantum of thermal conductance. Nature 404 (2000) 974-77.

11 S Murad, IK Puri: Thermal transport across nanoscale solid-fluid interfaces. Applied Physics Letters 92 (2008) 133105.

12 J Koplik, JR Banavar, JF Willemsen: Molecular-Dynamics of Fluid-Flow at Solid-Surfaces. Physics of Fluids A-Fluid Dynamics 1 (1989) 781-94.

13 S Murad, IK Puri: Dynamics of nanoscale jet formation and impingement on flat surfaces. Physics of Fluids 19 (2007) 128102.

14 L Xue, P Keblinski, SR Phillpot, SUS Choi, JA Eastman: Two regimes of thermal resistance at a liquid-solid interface. Journal of Chemical Physics 118 (2003) 337-39.

15 YC Liu, Q Wang: Transport behavior of water confined in carbon nanotubes. Physical Review B 72 (2005).

16 S. Merabia, P. Keblinski, L. Joly, L.J. Lewis, J.L. Barrat, Physical Review E 79/2 (2009).

17 S Murad, J Lin: Molecular modeling of fluid separations using membranes: effect of molecular forces on mass transfer rates. Chemical Engineering Journal 74 (1999) 99-108.

18 S Murad, J Lin: Using thin zeolite membranes and external electric fields to separate supercritical aqueous electrolyte solutions. Industrial & Engineering Chemistry Research 41 (2002) 1076-83.

19 IP Swainson, MT Dove: Molecular-dynamics simulation of alpha-cristobalite and beta-cristobalite. Journal of Physics-Condensed Matter 7 (1995) 1771-88.

20 DJ Evans, S Murad: Singularity free algorithm for molecular-dynamics simulation of rigid polyatomics. Molecular Physics 34 (1977) 327-31.

21 MP Allen, DJ Tildesley: Computer Simulation of Liquids Clarendon Press, Oxford, 1987.

22 S Murad, IK Puri: Nanoscale jet collision and mixing dynamics. Nano Letters 7 (2007) 707-12.

23 J Chandrasekhar, SF Smith, WL Jorgensen: SN2 reaction profiles in the gas-phase and aqueous-solution. Journal of the American Chemical Society 106 (1984) 3049-50.

24 FH Stillinger, TA Weber: Computer-simulation of local order in condensed phases of silicon. Physical Review B 31 (1985) 5262-71.

25 IG Tironi, R Sperb, PE Smith, WF Vangunsteren: A generalized reaction field method for molecular-dynamics simulations. Journal of Chemical Physics 102 (1995) 5451-59.

26 HJC Berendson, J Postma, WF van Gunsteren, in B. Pullman (Ed.), Intermolecular Forces. Reidel, Dordecht, 1981.

27 R Gargallo, PH Hunenberger, FX Aviles, B Oliva: Molecular dynamics simulation of highly charged proteins: Comparison of the particle-particle particle-mesh and reaction field methods for the calculation of electrostatic interactions. Protein Science 12 (2003) 2161-72.

28 RO Watts: Monte Carlo studies of liquid water. Molecular Physics 28 (1974) 1069-83.

29 ER Cruz-Chu, A Aksimentiev, K Schulten: Water-silica force field for simulating nanodevices. Journal of Physical Chemistry B 110 (2006) 21497-508.

30 JG Yu, SR Phillpot, SB Sinnott: Interatomic potential for the structure and energetics of tetrahedrally coordinated silica polymorphs. Physical Review B 75 (2007).

31 IAPWS: Revised Release on the IAPS Formulation 1985 for the Thermal Conductivity of Ordinary Water Substance, International Association for the Properties of Water and Steam, London, 1998.

[32] http://webbook.nist.gov/chemistry/fluid/

33 A Saul, W Wagner: A fundamental equation for water covering the range from the melting line to 1273-K at pressures up to 25000 MPA. Journal of Physical and Chemical Reference Data 18 (1989) 1537-64.

34 W Wagner, A Pruss: The IAPWS formulation 1995 for the thermodynamic properties of ordinary water substance for general and scientific use. Journal of Physical and Chemical Reference Data 31 (2002) 387-535.

35 S. Murad and I. K. Puri, "Molecular simulation of thermal transport across hydrophilic interfaces," Chemical Physics Letters 467 (1-3), 110-113 (2008)

36 Balasubramanian, G., S. Banerjee, and I.K. Puri, Unsteady nanoscale thermal transport across a solid-fluid interface. Journal of Applied Physics, 2008. 104(6).

37 H.R. Shanks, P.D. Maycock, P.H. Sidles, G.C. Danielson, Physical Review 130/5 (1963) 1743.

38 S. Murad and I. K. Puri, "Thermal transport through a fluid–solid interface," Chemical Physics Letters, 476 (2009) 267-70.

39 S. Murad and I.K. Puri, "Thermal Transport Through Superlattice Solid-Solid Interfaces", Applied Physics Letters, 95 (2009) 051907.

40 Balasubramanian, G., and I. K. Puri, Heat conduction across a solid-solid interface: Understanding nanoscale interfacial effects on thermal resistance. Applied Physics Letters, 2011. 99:013116.

41 Cahill, D.G., W.K. Ford, K.E. Goodson, G.D. Mahan, A. Majumdar, H.J. Maris, R. Merlin, and S.R. Phillpot, Nanoscale thermal transport. Journal of Applied Physics, 2003. 93(2): p. 793-818.

42 Lee, S.M., D.G. Cahill, and R. Venkatasubramanian, Thermal conductivity of Si-Ge superlattices. Applied Physics Letters, 1997. 70(22): p. 2957-2959.

43 Borca-Tasciuc, T., W.L. Liu, J.L. Liu, T.F. Zeng, D.W. Song, C.D. Moore, G. Chen, K.L. Wang, M.S. Goorsky, T. Radetic, R. Gronsky, T. Koga, and M.S. Dresselhaus, Thermal conductivity of symmetrically strained Si/Ge superlattices. Superlattices and Microstructures, 2000. 28(3): p. 199-206.

44 A Nitzan: Chemistry - Molecules take the heat. Science 317 (2007) 759-60.

45 LJ Challis, K Dransfeld, J Wilks: Heat Transfer Between Solids and Liquid Helium II. Proceedings of the Royal Society of London. Series A, Mathematical and Physical Sciences 260 (1961) 31-46.